

# Wavelet Packet-Based Diffusion Model for Ground Motion Generation with Multi-Conditional Energy and Spectral Matching

Yi Ding<sup>1</sup> | Su Chen<sup>2</sup> | Jinjun Hu<sup>1,3</sup> | Xiaohu Hu<sup>2</sup> | Qingxu Zhao<sup>2</sup> | Xiaojun Li<sup>2,4</sup>

<sup>1</sup>National Key Laboratory of Precision Blasting, Jianghan University, Wuhan, 430056, China

<sup>2</sup>Key Laboratory of Urban Security and Disaster Engineering of the Ministry of Education, Beijing University of Technology, Beijing, 100124, China

<sup>3</sup>Key Laboratory of Earthquake Engineering and Engineering Vibration, China Earthquake Administration, Harbin, 150080, China

<sup>4</sup>Institute of Geophysics, China Earthquake Administration, Beijing, 100081, China

## Correspondence

Su Chen (Email: chensuchina@126.com)  
Jinjun Hu (Email: hu-jinjun@163.com)

## Abstract

Temporal energy distribution strongly affects nonlinear structural response and cumulative damage. We propose a multi-conditional diffusion framework for ground motion synthesis that simultaneously matches temporal energy evolution and target response spectra. Wavelet packet decomposition provides the signal representation and enables direct waveform reconstruction via orthogonal filter banks. A Transformer-based conditional encoder with cross-attention integrates heterogeneous conditions, including spectral ordinates, Arias intensity, temporal parameters, and Husid curves. The framework adopts the Elucidating Diffusion Model (EDM) with second-order Heun sampling to improve inference efficiency without sacrificing quality. Tests on the NGA-West2 database show that explicit temporal-energy constraints markedly improve control of energy onset and significant duration while preserving spectrum matching and maintaining stable diversity sampling. The framework yields spectrum-compatible motions with realistic energy evolution and supports uncertainty quantification via conditional diversity sampling.

## KEY WORDS

Ground motion synthesis, Diffusion models, Wavelet packet transform, Energy nonstationarity, Response spectrum matching, Cross-attention mechanism

## HIGHLIGHTS

- Integrates response spectrum, energy parameters, and Husid curves for ground motion synthesis
- Enables direct waveform reconstruction from wavelet packet coefficients via orthogonal filter banks
- Uses a variance-exploding EDM with a second-order Heun sampler for efficient, accurate generation

## 1 | INTRODUCTION

Performance-based seismic design and assessment require extensive ground motion records for nonlinear time-history analysis to evaluate structural dynamic responses and damage potential under various seismic hazard scenarios<sup>1,2</sup>. Although existing strong-motion databases have accumulated a large number of observed records<sup>3</sup>, their distribution in parameter space remains largely imbalanced. For engineering scenarios demanding specific combinations, such as large-magnitude near-field conditions, particular site classifications under maximum considered earthquakes, or simultaneous satisfaction of multiple intensity parameter constraints, observations are often insufficient for direct use.

Early spectral matching methods employed frequency-domain approaches. These methods adjust the Fourier amplitude spectrum based on the ratio of the target response spectrum to the time-history response spectrum, while keeping the Fourier phase of the reference time-history unchanged<sup>4</sup>. Another approach adds wavelets in the time domain to the initial time history, which often preserves the nonstationary characteristics of the reference time history<sup>5,6,7</sup>. With advances in nonstationary signal analysis, methods such as wavelet transform<sup>8,9,10</sup>, wavelet packet transform<sup>11,12,13</sup>, and Hilbert-Huang transform<sup>14,15</sup> have been introduced to better describe the nonstationarity of ground motion amplitude and frequency. Generating ground motions that

are compatible with a target response spectrum is an inherently ill-posed inverse problem. Mathematically, multiple distinct acceleration time histories may satisfy the same spectral target while differing significantly in physical characteristics such as amplitude envelope, duration, and temporal evolution of energy. Therefore, ground motion selection and synthesis should consider multiple intensity measures<sup>16,17</sup>.

Recent advances in deep learning have opened new pathways for ground motion generation. Generative models learn probabilistic mappings from control parameters to time-series samples by modeling high-dimensional stochastic distributions<sup>18,19,20</sup>, thereby avoiding iterative fitting procedures in traditional methods. Physics-based numerical simulation of ground motions is still constrained to low-frequency bands because of computational cost and limited small-scale medium characterization, so researchers have explored neural network approaches to generate broadband motions from low-frequency simulations<sup>21,22,23</sup>. However, these approaches still depend on random phase generation or low-frequency simulation accuracy, limiting control of high-frequency waveform characteristics. Generative adversarial networks (GANs) and their variants have been extensively applied to seismic waveform synthesis, enabling end-to-end generation by learning mappings between physical parameters (source, path, site) and waveforms<sup>24,25,26</sup>, generating response spectrum-conditioned artificial acceleration records<sup>27,28,29</sup>, and synthesizing aftershock time histories from mainshock records<sup>30,31</sup>. Variational autoencoders (VAEs) have also been introduced to this domain, with Ren et al.<sup>32</sup> learning amplitude information in the time-frequency domain while implicitly modeling wave propagation through geospatial coordinates, demonstrating superior training stability compared to GANs.

As an emerging generative framework, diffusion models have produced high-fidelity and diverse samples in computer vision and audio processing<sup>20,33,34,35</sup>. Recent research has used diffusion models to learn complex dynamical systems, enabling reconstruction and prediction of full spatiotemporal dynamics fields<sup>36,37,38,39</sup>. Compared to GANs, diffusion models are more stable to train, integrate multimodal conditions, and generate samples that balance diversity and fidelity. With explicit noise-prediction objectives and progressive denoising, diffusion models capture complex ground motion distributions and produce samples whose statistics closely match observations. Recent studies have applied diffusion models to ground motion generation, including denoising diffusion probabilistic models (DDPMs), multi-label conditional embedding, and latent space diffusion, achieving high-resolution seismic waveform synthesis<sup>40,41,42,43</sup>. Nevertheless, most approaches rely on scalar conditions such as magnitude and distance, providing limited control over temporal energy distribution and other nonstationary characteristics. For nonlinear structural response analysis, ground motions sharing an identical response spectrum but differing in energy evolution processes can induce markedly different damage accumulation effects.

To address these limitations, this study proposes a multi-conditional ground motion generation framework based on the Elucidating Diffusion Model (EDM) proposed by Karras et al.<sup>44</sup>. This framework jointly constrains spectral and energy-evolution characteristics by using a comprehensive conditional set that includes the response spectrum, Arias intensity, energy time parameters, and the Husid curve. Wavelet packet decomposition maps waveforms into multiscale time-frequency representations. Based on orthogonal filter banks, time-domain waveforms are reconstructed directly from generated wavelet coefficients, avoiding iterative phase retrieval. A lightweight Transformer-based conditional encoder<sup>45</sup> captures multi-source conditional coupling, and conditional information is injected into the denoising process through cross-attention in the U-Net architecture<sup>46</sup>. During inference, a second-order Heun sampler improves efficiency while maintaining generation quality. We validate the method by evaluating intensity-parameter control, time-domain waveform similarity, and uncertainty.

## 2 | METHODOLOGY

Figure 1 summarizes the multi-conditional diffusion framework for generating constrained seismic waveforms. It includes three components:

- Wavelet packet decomposition and reconstruction that interact with both training and generation phases of the diffusion model.
- A Transformer-based conditional encoder for multi-source condition fusion, with cross-attention injection in multi-scale attention layers.
- An EDM-based U-Net denoiser trained in normalized wavelet packet coefficient space; during inference, a second-order Heun sampler generates samples from Gaussian noise, which are reconstructed into time-domain waveforms via inverse wavelet packet transform.

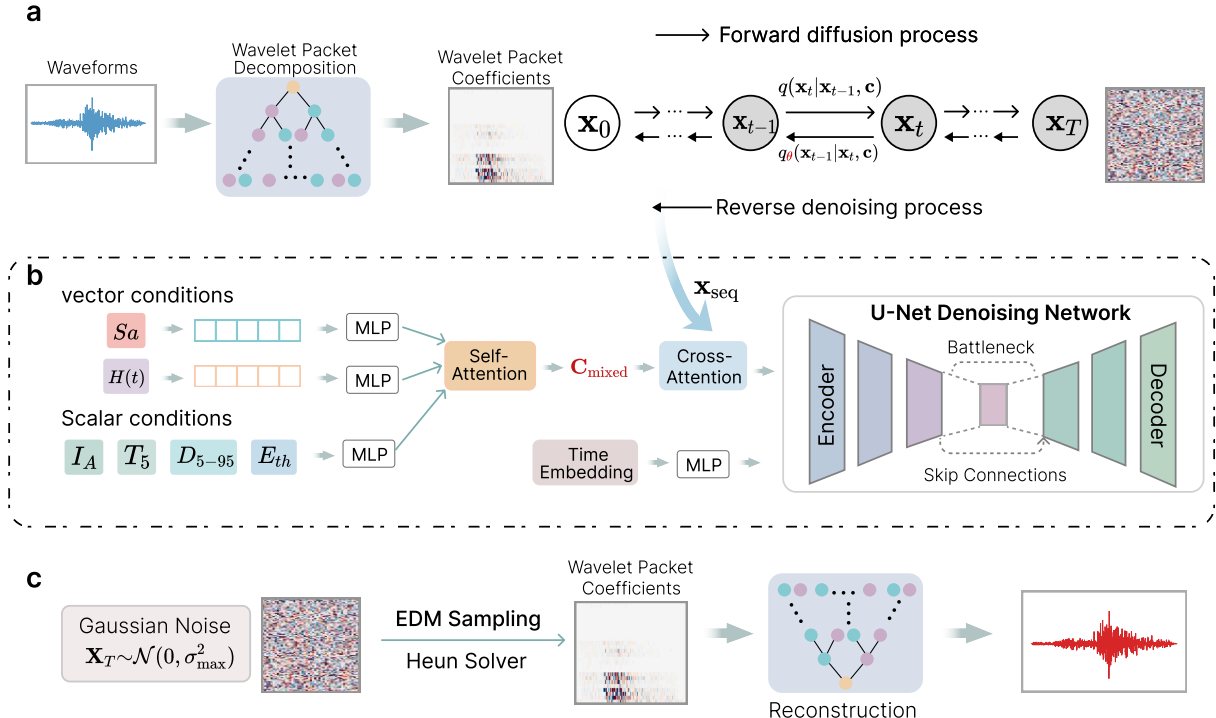


**FIGURE 1** Multi-conditional diffusion framework for constrained ground motion generation: (a) wavelet packet decomposition and diffusion in coefficient space; (b) conditional encoder fuses vector conditions ( $S_a$ ,  $H(t)$ ) and scalar IMs ( $I_A$ ,  $T_5$ ,  $D_{5-95}$ ,  $E_{th}$ ), and injects them into a U-Net denoiser via cross-attention; (c) EDM sampling (Heun solver) from Gaussian noise followed by inverse wavelet packet reconstruction to obtain time-domain waveforms.

## 2.1 | Wavelet Packet Representation

Generative models must capture long-range temporal dependencies and transient local details in complex waveforms. Using high-dynamic-range, long-sequence time-domain seismic signals as training targets challenges training stability and generalization. To capture nonstationary characteristics and align with diffusion models in continuous representation spaces, previous studies<sup>25,40,47</sup> typically learn time-frequency spectrograms from the short-time Fourier transform (STFT) and reconstruct waveforms via phase retrieval methods such as the Griffin-Lim algorithm.

This work uses Daubechies-6 (Db6) wavelet packet multiresolution decomposition<sup>48,49</sup> as the signal representation, enabling direct time-domain waveform reconstruction from generated wavelet coefficients via orthogonal filter banks and avoiding iterative phase recovery. For an acceleration sequence  $a[n]$  of length 16,384 points, a 7-level decomposition using the Db6 wavelet yields  $2^7 = 128$  frequency subband nodes, each containing 128 time-domain coefficients, forming a  $128 \times 128$  two-dimensional representation. The recursive decomposition is implemented through low-pass and high-pass filters:

$$WP_{\ell+1,2k}[m] = \sum_n h[2m-n]WP_{\ell,k}[n], \quad WP_{\ell+1,2k+1}[m] = \sum_n g[2m-n]WP_{\ell,k}[n], \quad (1)$$

where  $h[n]$  and  $g[n]$  denote the low-pass and high-pass decomposition filters of the Db6 wavelet, respectively,  $m$  represents the time index after downsampling,  $\ell$  denotes the decomposition level, and  $k$  indexes nodes at each level.

We normalize coefficients at each node independently. For the  $k$ -th node coefficients  $\mathbf{w}_k$ , normalization yields  $\tilde{\mathbf{w}}_k = (\mathbf{w}_k - \mu_k)/(\sigma_k + \epsilon)$ , where  $\mu_k$  and  $\sigma_k$  denote the mean and standard deviation, respectively, and  $\epsilon = 10^{-6}$  prevents division by zero.

During inference, waveforms are reconstructed via inverse wavelet packet transform. Starting from the 128 nodes at level 7, synthesis proceeds layer-by-layer through reconstruction filters  $\tilde{h}[n]$  and  $\tilde{g}[n]$ :

$$WP_{\ell-1,k}[n] = \sum_m (\tilde{h}[n-2m]WP_{\ell,2k}[m] + \tilde{g}[n-2m]WP_{\ell,2k+1}[m]). \quad (2)$$

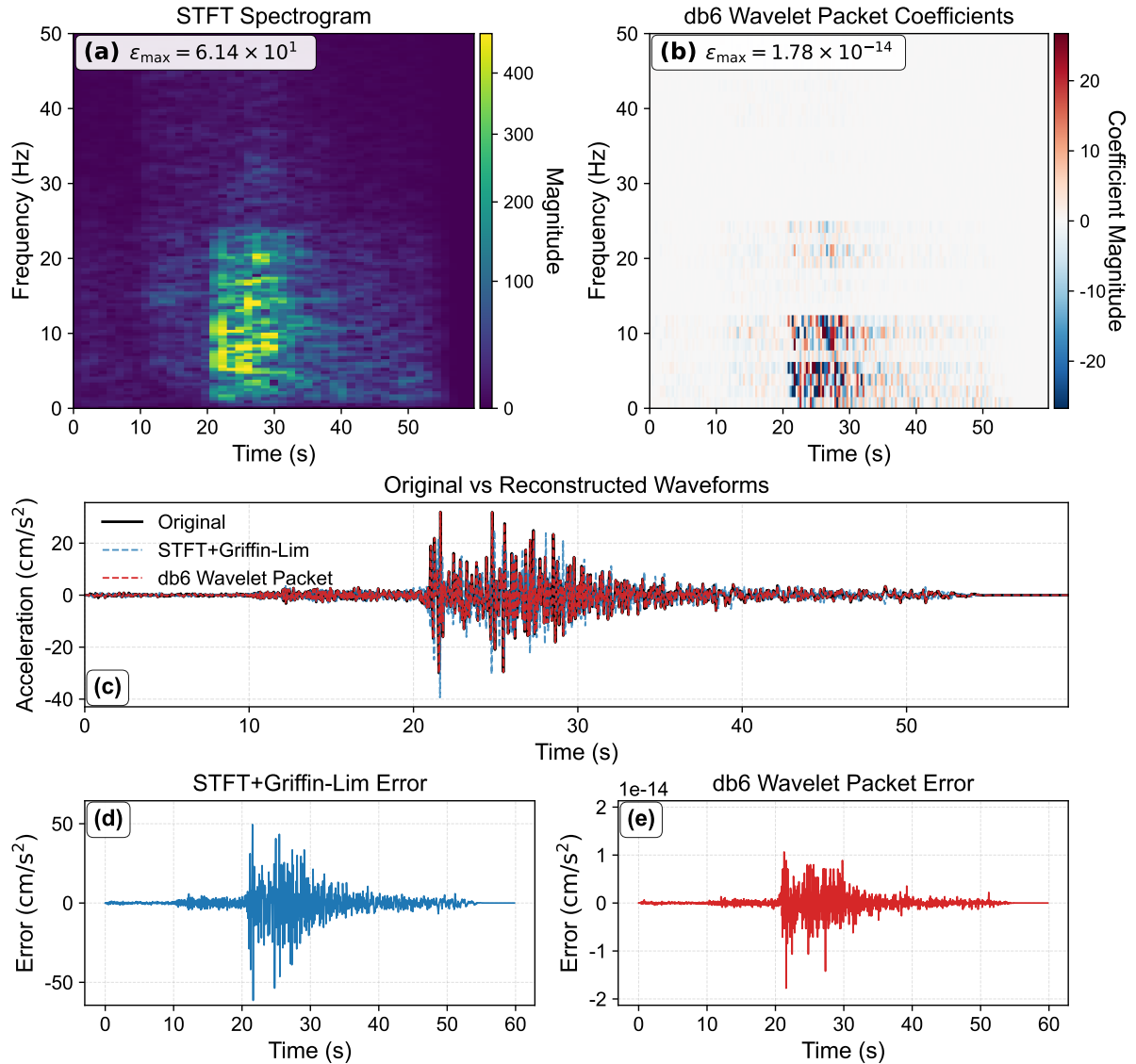


**FIGURE 2** Comparison between STFT+Griffin-Lim and wavelet packet reconstruction. (a) STFT spectrogram with maximum reconstruction error  $\varepsilon_{\max} = 6.14 \times 10^1$ ; (b) Wavelet packet coefficients with  $\varepsilon_{\max} = 1.78 \times 10^{-14}$ ; (c) original waveform (black) compared with STFT+Griffin-Lim reconstruction (blue dashed) and wavelet packet reconstruction (red dashed); (d) STFT+Griffin-Lim reconstruction error; (e) Wavelet packet reconstruction error.

where the synthesis filters  $\tilde{h}[n]$  and  $\tilde{g}[n]$  satisfy the perfect reconstruction conditions with the corresponding decomposition filters.

Compared to traditional STFT-based methods, wavelet packet representation offers several advantages in ground motion generation. Figure 2 presents a direct comparison between STFT+Griffin-Lim and wavelet packet reconstruction on a representative seismic record. The wavelet packet approach offers three advantages: (1) reconstruction precision, achieving errors on the order of  $10^{-14}$  to  $10^{-15}$ , which is a significant improvement over Griffin-Lim reconstruction errors; (2) computational efficiency, enabling single-pass reconstruction via orthogonal filter banks and eliminating Griffin-Lim's iterative phase recovery (128 iterations in this test); and (3) phase preservation, because wavelet packet decomposition is a linear transform with perfect reconstruction, whereas Griffin-Lim approximates phase via iterative magnitude-only optimization. These advantages make wavelet packet representation particularly suitable for generative modeling, where reconstruction fidelity directly impacts the quality of synthesized ground motions.

## 2.2 | Diffusion Model Theory

Diffusion models learn data distributions through progressive noising and denoising. This study adopts the Elucidating Diffusion Model (EDM) framework proposed by Karras et al.<sup>44</sup>, which defines a design space for diffusion models by systematically decoupling components including noise scheduling, network preconditioning, loss weighting, and sampling algorithms, thereby achieving superior performance in generative tasks.

Let the data distribution be denoted as  $p_{\text{data}}(\mathbf{x})$  with variance  $\sigma_{\text{data}}^2$ . For conditional generation tasks, the data distribution is represented as a mixture distribution of conditional parameters:

$$p_{\text{data}}(\mathbf{x}) = \mathbb{E}_{p_{\text{cond}}(\mathbf{c})}[p_{\text{data}}(\mathbf{x}|\mathbf{c})], \quad (3)$$

where  $\mathbf{c}$  denotes the conditional parameters. Adding Gaussian noise with variance  $\sigma^2$  yields a family of noisy distributions  $p(\mathbf{x}; \sigma)$ . When the noise standard deviation is sufficiently large ( $\sigma_{\text{max}} \gg \sigma_{\text{data}}$ ),  $p(\mathbf{x}; \sigma_{\text{max}})$  approximates a pure noise distribution.

For the forward noising process, adding Gaussian noise with standard deviation  $\sigma$  to clean data  $\mathbf{x}_0$  yields the noisy sample:

$$\mathbf{x}_t = \mathbf{x}_0 + \sigma \epsilon, \quad \epsilon \sim \mathcal{N}(0, \mathbf{I}), \quad (4)$$

where  $t$  denotes a general index for the noisy state,  $\sigma$  represents the noise level, and the transition kernel is  $p(\mathbf{x}_t|\mathbf{x}_0) = \mathcal{N}(\mathbf{x}_t|\mathbf{x}_0, \sigma^2 \mathbf{I})$ .

The core concept of diffusion models is to start from pure Gaussian noise sampled at the maximum noise level  $\sigma_{\text{max}}$  and progressively denoise to generate clean samples conforming to the target distribution  $p_{\text{data}}(\mathbf{x}|\mathbf{c})$ . We discretize the denoising process into  $T$  steps, starting from  $\mathbf{x}_T \sim \mathcal{N}(0, \sigma_{\text{max}}^2 \mathbf{I})$  and iteratively updating to  $\mathbf{x}_0$ . The noise level  $\sigma$  is sampled from a log-normal distribution ( $\ln \sigma \sim \mathcal{N}(P_{\text{mean}}, P_{\text{std}}^2)$  with  $P_{\text{mean}} = -1.2$  and  $P_{\text{std}} = 1.2$  in this study), to balance learning across noise scales ( $\sigma \in [0.002, 80]$ ).

During training, the diffusion model employs the denoising score matching objective function. This approach circumvents computation of normalization constants by directly learning the score function  $\nabla_{\mathbf{x}} \log p(\mathbf{x}; \sigma)$  from noisy data. The denoising function  $D(\mathbf{x}; \sigma)$  minimizes the  $L_2$  denoising error:

$$\mathcal{L} = \mathbb{E}_{\sigma, \mathbf{y}, \mathbf{n}} \left[ \lambda(\sigma) \|D(\mathbf{y} + \mathbf{n}; \sigma) - \mathbf{y}\|_2^2 \right], \quad (5)$$

where  $\sigma \sim p_{\text{train}}$ ,  $\mathbf{y} \sim p_{\text{data}}$ ,  $\mathbf{n} \sim \mathcal{N}(\mathbf{0}, \sigma^2 \mathbf{I})$ . The weighting function  $\lambda(\sigma) = (\sigma^2 + \sigma_{\text{data}}^2)/(\sigma \cdot \sigma_{\text{data}})^2$  (with  $\sigma_{\text{data}} = 0.5$  in this study) ensures uniform loss weighting across different noise levels, avoiding training bias toward specific noise scales. Thus the score matching relation holds:

$$\nabla_{\mathbf{x}} \log p(\mathbf{x}; \sigma) = \frac{D(\mathbf{x}; \sigma) - \mathbf{x}}{\sigma^2}. \quad (6)$$

The key observation of diffusion models is that  $D(\mathbf{x}; \sigma)$  can be trained using a neural network  $D_{\theta}(\mathbf{x}; \sigma)$ . To maintain network inputs and outputs within stable numerical ranges, EDM introduces skip connections and scaling preconditioning mechanisms. The denoising network  $D_{\theta}$  is constructed as:

$$D_{\theta}(\mathbf{x}, \sigma) = c_{\text{skip}}(\sigma) \mathbf{x} + c_{\text{out}}(\sigma) F_{\theta}(c_{\text{in}}(\sigma) \mathbf{x}, c_{\text{noise}}(\sigma)), \quad (7)$$

where  $F_{\theta}$  denotes the U-Net backbone network.  $c_{\text{skip}}(\sigma)$  modulates the skip connection,  $c_{\text{in}}(\sigma)$  and  $c_{\text{out}}(\sigma)$  scale the input and output magnitudes, and  $c_{\text{noise}}(\sigma)$  maps noise level  $\sigma$  into a conditioning input for  $F_{\theta}$ .

The scaling functions are derived through the following principles: (1) network inputs possess unit variance; (2) training targets possess unit variance; (3) minimization of network error amplification coefficients; (4) uniform distribution of loss weights across different noise levels. The derivation yields:

$$\begin{cases} c_{\text{skip}}(\sigma) &= \sigma_{\text{data}}^2 / (\sigma^2 + \sigma_{\text{data}}^2) \\ c_{\text{out}}(\sigma) &= \sigma \cdot \sigma_{\text{data}} / \sqrt{\sigma_{\text{data}}^2 + \sigma^2} \\ c_{\text{in}}(\sigma) &= 1 / \sqrt{\sigma_{\text{data}}^2 + \sigma^2} \\ c_{\text{noise}}(\sigma) &= \frac{1}{4} \ln(\sigma) \end{cases} \quad (8)$$

We can equivalently express the loss (Eq. 5) with respect to the raw network output  $F_\theta$  in Eq. 7:

$$\mathcal{L} = \mathbb{E}_{\sigma, \mathbf{y}, \mathbf{n}} [\underbrace{\lambda(\sigma) c_{\text{out}}(\sigma)^2}_{\text{effective weight}} \underbrace{\| F_\theta(c_{\text{in}}(\sigma) \cdot (\mathbf{y} + \mathbf{n}); c_{\text{noise}}(\sigma)) - \underbrace{\frac{1}{c_{\text{out}}(\sigma)} (\mathbf{y} - c_{\text{skip}}(\sigma) \cdot (\mathbf{y} + \mathbf{n})) \|_2^2}_{\text{effective training target}}]. \quad (9)$$

During inference, starting from Gaussian noise  $\mathbf{x}_T \sim \mathcal{N}(0, \sigma_{\text{max}}^2 \mathbf{I})$ , a second-order Heun method is used to solve the ODE. Compared to the first-order Euler method, this significantly reduces discretization error for the same number of steps. This study adopts  $N = 25$  noise levels (corresponding to 50 network evaluations), substantially enhancing efficiency while maintaining generation quality compared to traditional DDPMs (1000 steps). This deterministic sampling yields unique solutions for a given condition and initial noise, facilitating subsequent analysis; diversity inference for uncertainty quantification can be achieved by varying the initial noise.

## 2.3 | Network Architecture

The core of the diffusion model is the parameterized denoising network for predicting clean data. This work adopts a U-Net-based architecture, comprising an encoder (downsampling path), a bottleneck layer, and a decoder (upsampling path), with skip connections that enable multi-scale feature fusion. The network uses 64 base channels with multipliers [1, 2, 4, 4], incorporating 2 residual blocks per resolution level. Attention mechanisms are positioned at the 8x downsampling rate feature map. This configuration balances model expressiveness with computational efficiency.

The network body consists of stacked residual blocks and attention blocks. Residual blocks incorporate normalization, activation functions, and convolution operations to achieve nonlinear feature transformations. Attention blocks integrate two attention mechanisms: self-attention and conditional cross-attention. Self-attention allows time-frequency positions within features to interact, learning long-range time-frequency dependencies. Cross-attention allows waveform features in the denoising process to interact with encoded conditional tokens, achieving conditional control over generated waveform intensity parameters and spectral characteristics.

In the diffusion process, different noise levels correspond to different denoising difficulties. To enable the denoising network to perceive the current noise state, noise level information is injected into the network. Noise levels are encoded via logarithmic transformation  $c_{\text{noise}}(\sigma) = \frac{1}{4} \ln \sigma$  (Eq. 8), then transformed into high-dimensional embedding vectors via sinusoidal position encoding:

$$\text{PE}(c_{\text{noise}}) = [\sin(\omega_1 c_{\text{noise}}), \cos(\omega_1 c_{\text{noise}}), \dots, \sin(\omega_{d/2} c_{\text{noise}}), \cos(\omega_{d/2} c_{\text{noise}})], \quad (10)$$

where  $\omega_i = 1/10000^{2i/d}$  for  $i \in \{0, 1, \dots, d/2 - 1\}$  represents predefined frequencies, and  $d$  denotes the embedding dimension. This encoding method generates continuous and smooth vector representations, enabling the network to perceive noise levels across different frequency resolutions. Within the U-Net architecture's residual blocks, noise embeddings are projected with an MLP to dimensions matching feature channel counts, then fused with features through element-wise addition, thereby adaptively modulating denoising behavior according to specific noise levels.

## 2.4 | Cross-Attention Conditional Injection

To precisely control the intensity and time-frequency characteristics of generated seismic waveforms, the diffusion model must receive additional conditioning information, which is encoded in a form that can be injected into the diffusion process. For scalar conditions (such as Arias intensity), MLPs directly project them into single tokens. For vector conditions (such as the response spectrum and the Husid curve), they are partitioned into patches and mapped to token sequences via MLPs, while positional encodings are added to each vector condition's tokens, enabling the model to understand the relative positions of tokens in sequences. For the response spectrum, positions represent progression from short to long periods. For the Husid curve, positions represent energy accumulation from early to late stages.

Simply encoding each condition separately would neglect coupling relationships among them. Therefore, we design a three-layer Transformer encoder. Each layer within the encoder contains a multi-head self-attention module (4 attention heads) and a position-wise feed-forward network, enabling conditional tokens to interact layer-by-layer and capture global conditional dependencies.

We introduce a cross-attention mechanism into the attention blocks of the U-Net encoder, bottleneck layer, and decoder. Cross-attention enables interaction between waveform features and conditional token sequences during the denoising process, achieving fine-grained conditional control over generation. We first flatten the input wavelet packet time-frequency representation into a sequence. For a time-frequency representation containing temporal and frequency information  $\mathbf{x} \in \mathbb{R}^{C \times H \times W}$ , this operation converts the two-dimensional feature map into a linear sequence  $\mathbf{x}_{\text{seq}} \in \mathbb{R}^{(H \cdot W) \times C}$ . Then, this waveform feature sequence is projected to obtain the query matrix:

$$\mathbf{Q} = \mathbf{x}_{\text{seq}} \mathbf{W}_Q \in \mathbb{R}^{(H \cdot W) \times d_k}. \quad (11)$$

Simultaneously, the token sequence  $\mathbf{C}_{\text{mixed}}$  output by the conditional encoder undergoes linear projection to obtain key ( $\mathbf{K}$ ) and value ( $\mathbf{V}$ ) matrices:

$$\mathbf{K} = \mathbf{C}_{\text{mixed}} \mathbf{W}_K \in \mathbb{R}^{N_c \times d_k}, \quad \mathbf{V} = \mathbf{C}_{\text{mixed}} \mathbf{W}_V \in \mathbb{R}^{N_c \times d_v}, \quad (12)$$

where  $N_c$  denotes the total number of conditional tokens, and  $\mathbf{W}_Q, \mathbf{W}_K, \mathbf{W}_V$  are learnable projection matrices.

The attention weights are computed via scaled dot-product between waveform feature queries and conditional token keys:

$$\text{Attn} = \text{softmax} \left( \frac{\mathbf{Q} \mathbf{K}^T}{\sqrt{d_k}} \right) \in \mathbb{R}^{(H \cdot W) \times N_c}. \quad (13)$$

The attention weights perform weighted summation on the value matrix ( $\mathbf{V}$ ) to yield attention output:  $\text{Attn} \cdot \mathbf{V} \in \mathbb{R}^{(H \cdot W) \times d_v}$ . The attention output is then linearly projected to match the channel dimension  $C$  and reshaped to spatial form  $\mathbb{R}^{C \times H \times W}$ , and the result is added back to the original features via residual connection.

Considering the complexity of condition-waveform feature interactions, we employ multi-head attention with four heads rather than single-head attention. Specifically, the channel dimension  $C$  is evenly split into four subspaces, with each head independently performing scaled dot-product attention to yield outputs of dimension  $d_v = C/4$ . Subsequently, outputs from all heads are concatenated and linearly projected back to the original channel dimension. This design enables the model to learn conditional-feature correlations in parallel from multiple perspectives, enhancing the model's capacity to capture complex conditional dependencies.

### 3 | DATABASE CONSTRUCTION AND PREPROCESSING

The training and testing datasets for this study are built from the NGA-West2 database<sup>3</sup> released by the Pacific Earthquake Engineering Research Center (PEER). Following PEER's rigorous quality control, we performed additional data integrity and validity checks, yielding 19,760 high-quality seismic acceleration records (the first horizontal component). The dataset is split into training and test sets with a 9:1 ratio, yielding 17,784 training records and 1,976 test records.

The data preprocessing pipeline comprises: (1) resampling to 100 Hz, where low-sampling-rate records are upsampled by linear interpolation and high-sampling-rate records are low-pass filtered and downsampled; (2) standardizing all record durations to 163.84 seconds (16,384 points) via truncation or zero-padding to match the  $128 \times 128$  wavelet packet representation described in Section 2.1; and (3) computing response spectra and key intensity parameters, followed by normalization.

We extract conditioning variables to match energy and spectral characteristics: scalar intensity measures including Arias intensity ( $I_A$ ), 5% energy arrival time ( $T_5$ ), significant duration ( $D_{5-95}$ ), and temporal centroid ( $E_{th}$ ); and vector parameters including the response spectrum and the Husid curve. Arias intensity reflects the total seismic energy, defined as:

$$I_A = \frac{\pi}{2g} \int_0^{T_d} a^2(t) dt, \quad (14)$$

where  $a(t)$  denotes the acceleration time history,  $T_d$  represents the total duration, and  $g$  is gravitational acceleration. Significant duration  $D_{5-95}$  is defined as the interval from the 5% cumulative energy moment ( $T_5$ ) to the 95% cumulative energy moment ( $T_{95}$ ), i.e.,  $D_{5-95} = T_{95} - T_5$ , characterizing the main energy-release phase of ground motion.

The temporal centroid ( $E_{th}$ ) describes the temporal center of seismic energy release<sup>11</sup>, defined as:

$$E_{th} = \frac{\int_0^{T_d} t \cdot a^2(t) dt}{\int_0^{T_d} a^2(t) dt}, \quad (15)$$

where the numerator is the time integral weighted by the square of acceleration, and the denominator represents the total energy.

The Husid function, equivalent to the normalized cumulative Arias intensity process, constrains the nonstationarity of acceleration time histories<sup>16</sup> and serves as a critical parameter describing seismic temporal-energy characteristics. Since Arias intensity is separately controlled as a scalar condition, the normalized Husid curve describes energy accumulation patterns:

$$H(t) = \frac{\int_0^t a^2(\tau) d\tau}{\int_0^{T_d} a^2(\tau) d\tau} \in [0, 1]. \quad (16)$$

The Husid curve is monotonic and smooth; therefore, it is downsampled to 256 discrete points uniformly distributed over the interval  $[0, T_d]$  to balance representation efficiency with feature completeness.

To reduce the influence of scale differences across conditioning variables, we normalize all parameters. For Arias intensity, whose values span multiple orders of magnitude, we apply a logarithmic transformation combined with min-max scaling. First, we apply  $u = \log(1 + x)$  to compress the dynamic range, then the values are mapped to the interval  $[-1, 1]$ :

$$x_{\text{norm}} = 2 \cdot \frac{u - u_{\min}}{u_{\max} - u_{\min}} - 1, \quad (17)$$

where  $u_{\min}$  and  $u_{\max}$  denote the minimum and maximum values after logarithmic transformation, respectively. This approach effectively compresses intensity parameters spanning multiple orders of magnitude while preserving monotonicity. For temporal parameters  $T_5$ ,  $D_{5-95}$ , and  $E_{th}$ , the same min-max scaling formula (Eq. 17) is applied without logarithmic transformation.

The response spectrum  $S_a(T)$  for each record is normalized by PGA to preserve spectral shape information. The Husid energy curve does not require normalization and can be directly used as a conditional variable.

## 4 | EXPERIMENTAL RESULTS AND ANALYSIS

To verify the impact of conditional information on generation quality, this study compares two conditional scenarios. Case 1 uses only the response spectrum normalized by PGA as the condition. Case 2 adopts the response spectrum ( $S_a$ ), Arias intensity ( $I_A$ ), 5% energy arrival time ( $T_5$ ), significant duration ( $D_{5-95}$ ), temporal centroid ( $E_{th}$ ), and Husid curve ( $H(t)$ ) as conditions.

The models were trained using the Adam optimizer with a learning rate of  $1 \times 10^{-4}$  and a batch size of 110. To stabilize the generation quality, an exponential moving average (EMA) was applied to the model parameters with a decay rate of 0.999. Training was conducted in a distributed manner across three NVIDIA A100 GPUs employing the Distributed Data Parallel (DDP) strategy and mixed precision (BF16) to enhance computational efficiency. Each model was trained for 100 epochs, requiring approximately 2.5 hours to complete. For inference, we utilized the second-order Heun sampler with 25 steps (equating to 50 network evaluations) to achieve a balance between sampling efficiency and output quality. The inference was performed on a single NVIDIA A100 GPU with a batch size of 256, processing the entire test set of 1,976 records in approximately 3 minutes.

### 4.1 | Intensity Parameter Control Precision Analysis

We perform single-pass inference (one sample per test condition) to evaluate control precision for scalar intensity parameters. Figure 3 presents intensity parameter comparison results for Case 1 and Case 2 models; solid red lines indicate ideal matching, dashed green lines indicate  $\pm$  one standard deviation, and annotations report  $r$  (Pearson correlation) and  $\sigma$  (residual standard deviation).

Regarding Arias intensity ( $I_A$ ), Case 1 achieved a high correlation of  $r = 0.990$  and a standard deviation of  $\sigma = 0.33$ , despite not being explicitly conditioned. This indicates that the model may implicitly infer overall energy characteristics through PGA and the response spectrum. In Case 2, after explicitly incorporating  $I_A$  as a condition, the correlation increased to  $r = 0.996$  and the standard deviation decreased to  $\sigma = 0.21$ , demonstrating that explicit energy constraints play a key role in improving the accuracy of total energy control.

Performance differences between the two cases are pronounced for temporal distribution parameters. For 5% energy arrival time ( $T_5$ ), Case 1 yields  $r = 0.053$  with a standard deviation  $\sigma = 0.40$ , indicating that without explicit constraints the model struggles to capture energy onset moments. By introducing  $T_5$  and the Husid curve as explicit conditions, the correlation in Case 2 improves to  $r = 0.982$ , with the standard deviation reduced to  $\sigma = 0.06$ .  $D_{5-95}$  and  $E_{th}$  exhibit similar trends. The results indicate that Case 2 significantly improves control accuracy of temporal nonstationary features, making it more suitable for parameterized ground motion synthesis in engineering applications.

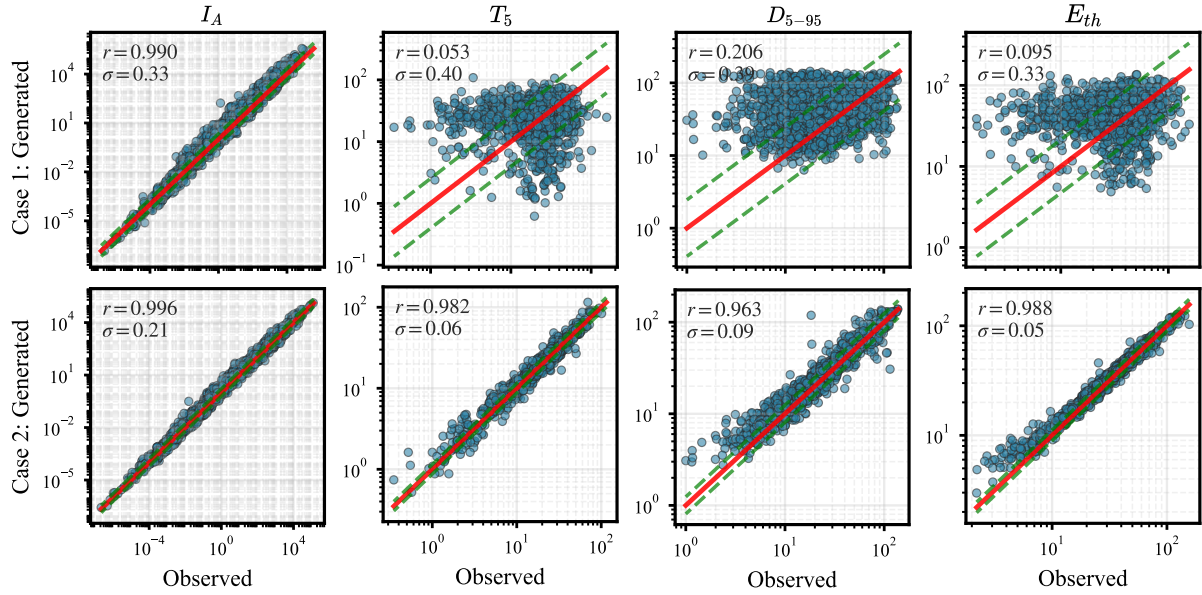


**FIGURE 3** Comparison of scalar intensity parameter control precision between Case 1 and Case 2.

For further validation, we randomly select 8 representative samples from the test set for waveform visualization. Figures 4 compare generated and observed waveforms for both cases, displaying waveforms up to the time corresponding to 99.5% cumulative Arias intensity. RSN denotes the unique record sequence number assigned to each record in the NGA-West2 database. In Case 1, generated waveform amplitude envelopes generally align with observed waveforms, reflecting ground motion nonstationarity, with main energy concentrated in central phases and decay characteristics at both ends. However, generated energy arrival times show noticeable deviations from observations, consistent with Case 1's low control precision over  $T_5$  in Figure 3.

After introducing the Husid curve and other conditioning information, Case 2 shows markedly improved agreement between generated and observed waveforms. Waveform comparisons reveal that the Case 2 model achieves high consistency with observed waveforms in both amplitude envelope and temporal energy distribution. Energy arrival times, main energy segments, and decay characteristics are substantially improved. This indicates that explicit temporal-energy constraints in Case 2 enhance waveform fidelity and mitigate the energy offset and unrealistic distribution issues present in Case 1.

Table 1 presents quantitative evaluation results for 8 representative samples under both conditioning configurations. For response spectrum matching, both cases demonstrate excellent performance with  $R^2$  values generally exceeding 0.95; however, for Husid curve matching, Case 2 exhibits significant advantages over Case 1, with all samples achieving  $R^2$  values exceeding 0.98.

**Table 1:** Response spectrum and Husid curve matching accuracy for representative samples

RSN	Case 1 $S_a$		Case 2 $S_a$		Case 1 $H(t)$		Case 2 $H(t)$	
	$R^2$	RMSE	$R^2$	RMSE	$R^2$	RMSE	$R^2$	RMSE
635	0.976	0.284	0.979	0.266	-0.309	0.364	0.984	0.022
2308	0.960	0.236	0.972	0.199	0.295	0.296	0.990	0.035
3572	0.950	0.215	0.958	0.197	0.084	0.265	0.997	0.015
8403	0.990	0.197	0.989	0.212	0.580	0.240	0.998	0.015
14702	0.983	0.346	0.988	0.287	0.909	0.123	0.997	0.021
15278	0.996	0.150	0.996	0.150	0.914	0.121	0.996	0.025
18231	0.993	0.134	0.993	0.134	0.933	0.109	0.998	0.021
20334	0.991	0.159	0.988	0.185	0.882	0.131	0.994	0.030

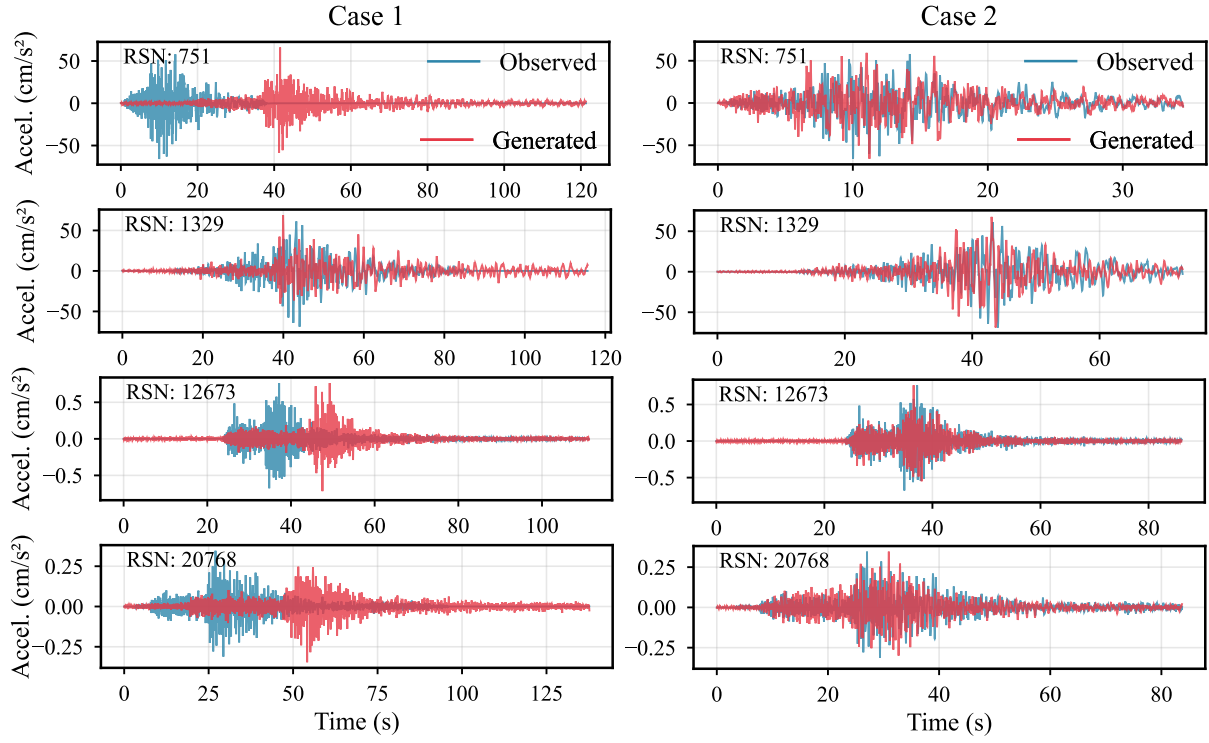


**FIGURE 4** Comparison of generated waveforms and observed waveforms for 8 representative samples from Case 1 and Case 2.

## 4.2 | Generation Uncertainty Analysis

Diffusion models can generate diverse samples under fixed conditions, which is important for quantifying uncertainties in structural response and fragility analysis. In this section, 150 conditional sets are randomly selected from the test dataset, and 100 distinct samples are generated for each condition. To evaluate the uncertainty and stability of the model outputs, the mean and standard deviation distributions of the generated samples are visualized and compared across both cases.

Figure 5 presents distributions of accuracy metrics for 15,000 generated samples for response spectrum and Husid curve matching. Accuracy evaluation employs coefficient of determination  $R^2$  and root mean square error (RMSE), defined as:

$$R^2 = 1 - \frac{\sum_{i=1}^n (y_{\text{obs},i} - y_{\text{gen},i})^2}{\sum_{i=1}^n (y_{\text{obs},i} - \bar{y}_{\text{obs}})^2}, \quad (18)$$

$$\text{RMSE} = \sqrt{\frac{1}{n} \sum_{i=1}^n (y_{\text{obs},i} - y_{\text{gen},i})^2}, \quad (19)$$

where  $y_{\text{obs},i}$  and  $y_{\text{gen},i}$  represent observed and generated values at the  $i$ -th point, respectively, and  $n$  denotes the number of data points. For the response spectrum,  $y = \log S_a$  (computed in logarithmic domain to balance weights across different period segments); for the Husid curve,  $y$  represents  $H(t)$  values directly computed from acceleration time histories.

In both cases, the  $R^2$  distribution of the response spectra is high, with 91% exceeding 0.9. The overlap of the distributions indicates that introducing additional time-energy distribution conditions does not affect the control accuracy of the response spectra. The RMSE distribution of the response spectra further reveals similar performance across various conditions, with the distribution peaks being essentially identical. In contrast, the  $R^2$  distribution of the Husid curves shows significant differences: Case 1 exhibits a relatively scattered distribution, with only 25% of the samples achieving  $R^2 > 0.90$ . Meanwhile, Case 2 displays a highly concentrated distribution, with over 88% of samples reaching  $R^2 > 0.90$ . This confirms that explicit Husid constraints substantially improve control of time-energy distribution. The RMSE distribution of the Husid curves further corroborates this conclusion.

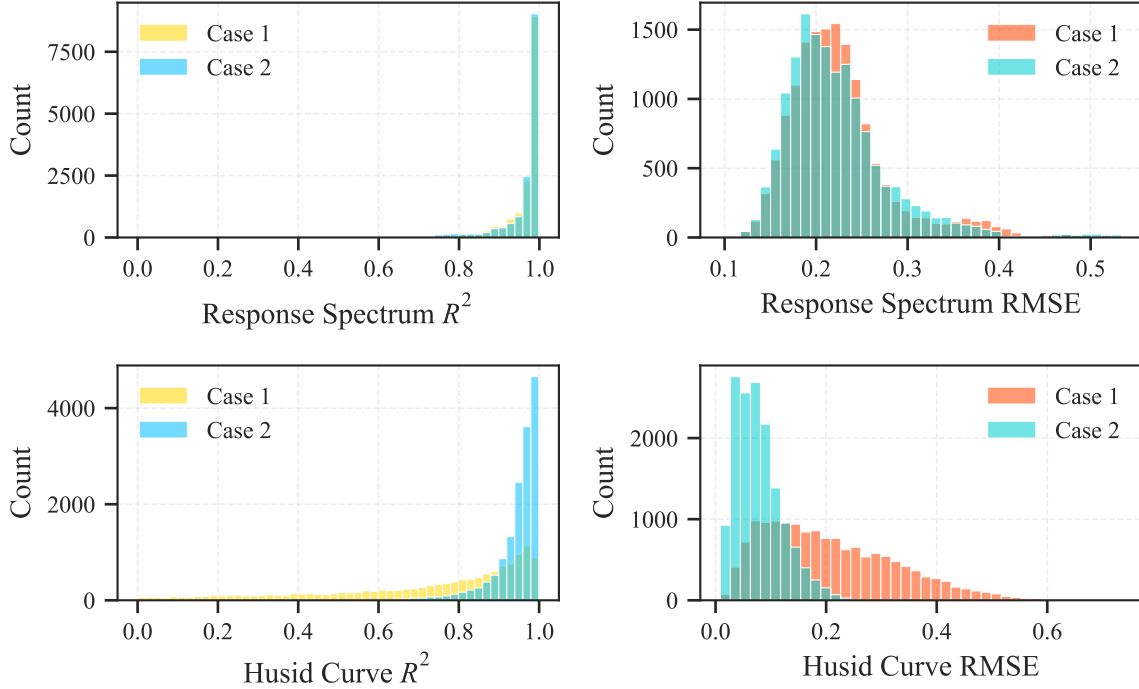


**FIGURE 5** Distribution histograms of accuracy metrics for 15,000 generated samples (150 conditions  $\times$  100 samples). Upper row: response spectrum  $R^2$  (left) and RMSE (right) distributions. Lower row: Husid curve  $R^2$  (left) and RMSE (right) distributions.

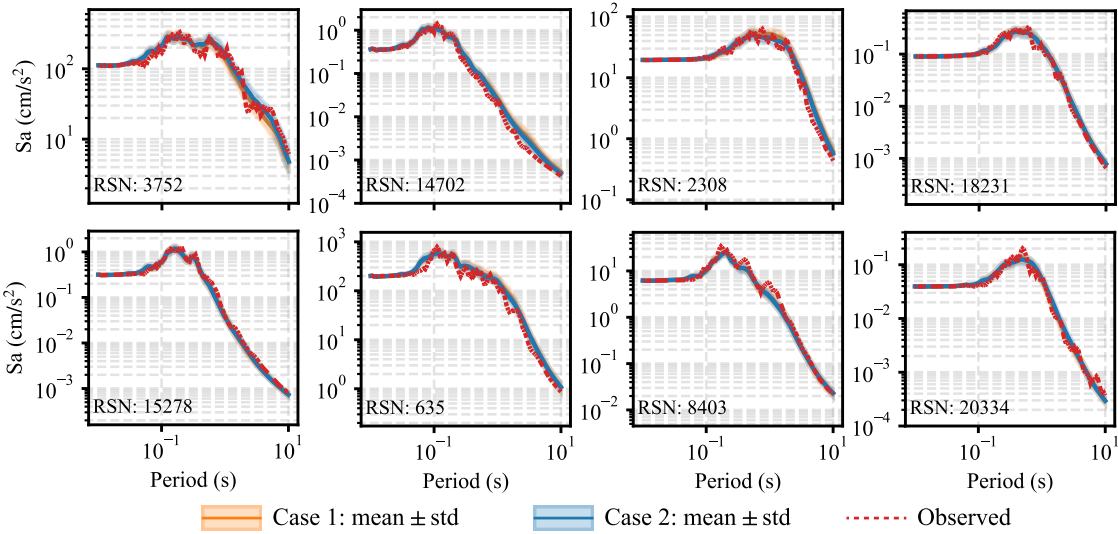


**FIGURE 6** Comparison of response spectrum matching uncertainty between Case 1 and Case 2.

Figure 6 contrasts Case 1 and Case 2 uncertainty in generated ground motion response spectrum matching. Results demonstrate that incorporating the response spectrum as an explicit condition effectively constrains spectral characteristics of generated motions. Both cases exhibit excellent response spectrum matching performance, with the mean response spectrum showing high agreement with the observed spectrum and demonstrating extremely low standard deviations. Standard deviation bands in the figure largely overlap across most period ranges for both cases, indicating that although Case 2 introduces additional constraint dimensions, it does not compromise response spectrum control precision.

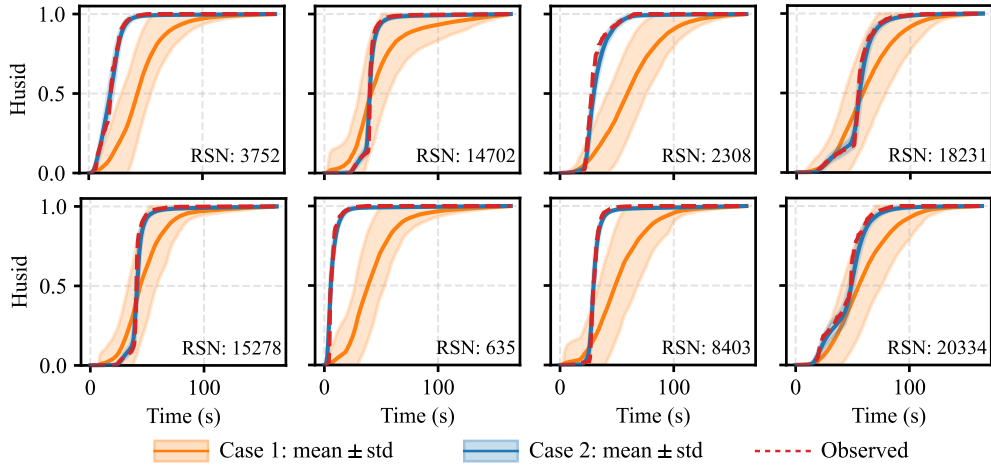


**FIGURE 7** Comparison of Husid curve matching between Case 1 and Case 2.

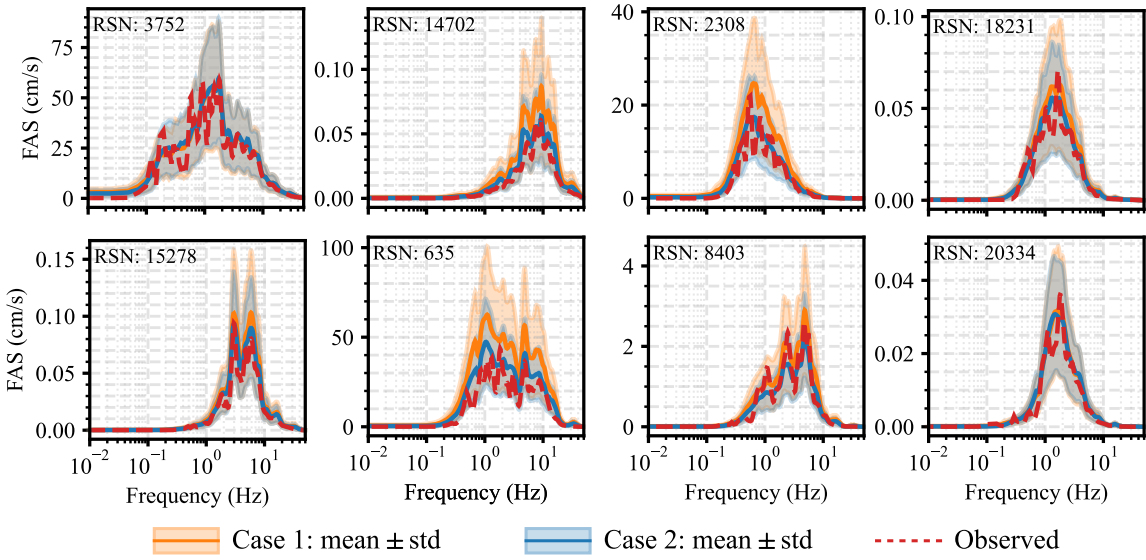


**FIGURE 8** Comparison of Fourier amplitude spectrum matching between Case 1 and Case 2.

Figure 7 further illustrates the comparison of Husid curve generation uncertainty between the two cases. In Case 1, generated samples generally preserve the monotonic physical trend, but standard deviations increase in the middle segment of energy accumulation, reflecting substantial uncertainty in energy release processes across samples. In contrast, Case 2, through explicit introduction of Husid curves as conditioning constraints, achieves mean curves highly aligned with observed values and markedly narrower standard deviation bands, demonstrating stability during critical energy accumulation phases.

Figure 8 further compares the Fourier amplitude spectrum (FAS) matching between both cases. Both Case 1 and Case 2 demonstrate good agreement with observed FAS, while Case 2 exhibits slightly narrower standard deviation bands in the intermediate frequency range, which corresponds to the dominant frequency content of most ground motions in the database. This suggests that explicit temporal energy constraints may indirectly enhance frequency content consistency by better regulating the temporal structure of generated waveforms.

To further quantify the influence of both conditional configurations on energy-related temporal parameter generation uncertainty, Figure 9 shows probability density estimates of scalar IMs for the representative sample RSN 2308 under stochastic inference with 100 realizations per case. The figure compares Case 1 (orange) and Case 2 (blue) across four critical parameters: Arias intensity ( $I_A$ ), 5% energy arrival time ( $T_5$ ), significant duration ( $D_{5-95}$ ), and temporal centroid ( $E_{th}$ ). The kernel density

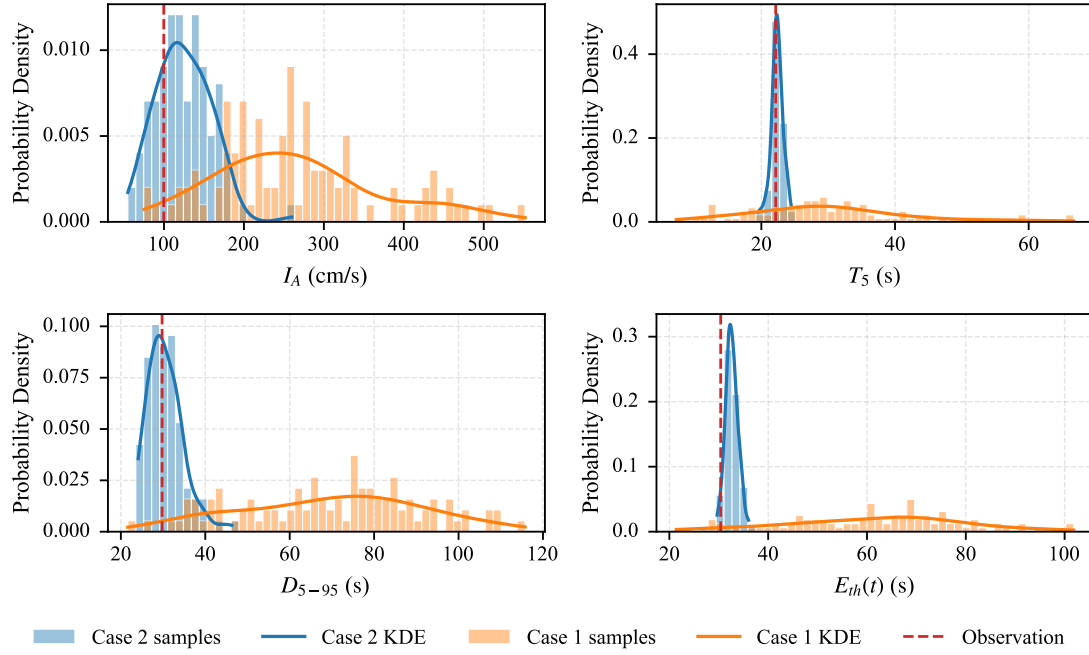


**FIGURE 9** Probability density distributions of intensity parameters for RSN 2308 under stochastic inference mode (100 samples per case).

estimation (KDE) curves of Case 1 for all four parameters exhibit flat profiles spanning wide ranges, indicating substantial dispersion. In contrast, Case 2 distributions are concentrated near the observed values (red dashed lines), indicating lower generation uncertainty across all energy-related temporal parameters.

This confirms that explicit temporal-energy constraints reduce generation uncertainty. By narrowing the feasible sample space, Case 2 ensures that stochastic realizations maintain consistent energy release patterns while matching the response spectrum, reducing uncertainty propagation in nonlinear structural response assessment.

## 5 | DISCUSSION

The proposed framework is computationally efficient through the variance-exploding diffusion formulation and second-order Heun sampler, requiring only 25 noise levels (50 network evaluations) compared to traditional DDPMs that typically demand 1000 steps. Further acceleration could be achieved with latent diffusion models (LDMs)<sup>34</sup>, which perform the denoising process in compressed latent spaces rather than high-dimensional wavelet coefficient spaces. Recent advances in single-step or few-step diffusion models, such as consistency models<sup>50,51</sup> and progressive distillation techniques<sup>52</sup>, suggest routes to real-time ground motion generation. However, the trade-off between inference speed and sample quality warrants careful study, particularly for capturing subtle temporal-energy characteristics that affect structural damage accumulation.

Future work can incorporate seismological parameters (magnitude, epicentral distance, focal depth, fault mechanism, etc.) to generate physical constraints consistent with ground motion prediction equations (GMPEs). This facilitates the synthesis of site-specific ground motions for performance-based seismic engineering. Potential applications also include matching multi-damping response spectra and jointly generating three-component spectrum-compatible ground motions.

The selection of conditioning parameters in this study is motivated by their established importance in earthquake engineering practice. The proposed conditional encoding architecture is scalable. The modular Transformer encoder can readily accommodate additional parameters such as peak ground velocity (PGV), cumulative absolute velocity (CAV), or frequency content metrics through expansion of token sequences. Furthermore, the cross-attention mechanism naturally handles variable-length condition

sets, allowing practitioners to select conditioning parameters based on specific application requirements without architectural modifications.

While this framework demonstrates promising performance on the NGA-West2 database, several limitations warrant acknowledgment. The model's generalization to ground motions beyond the training distribution (e.g., extremely long-period pulse-like motions, near-fault directivity effects, or basin-induced surface waves) requires further validation. The wavelet packet representation, though offering perfect reconstruction, assumes fixed time-frequency resolution across all scales, which may be suboptimal for ground motions with highly transient features. Additionally, the current implementation operates on single-component horizontal motions with standardized duration, potentially limiting applicability to very short or extended duration scenarios. The relationship between conditioning parameter accuracy and downstream structural response prediction also warrants systematic investigation, as small deviations in temporal energy characteristics may amplify through nonlinear structural dynamics. Future work should explore transfer learning strategies to adapt the trained model to different regional databases and incorporate physics-based constraints to enhance extrapolation capability beyond empirical data distributions.

## 6 | CONCLUSIONS

This study presents a multi-conditional diffusion model framework for ground motion generation that jointly matches the response spectrum and temporal energy characteristics. By employing wavelet packet representation with perfect reconstruction, Transformer-based conditional encoding, and cross-attention mechanisms, the framework achieves precise control over both spectral and energy evolution features. Comparative experiments conducted using the NGA-West2 database demonstrate that this methodology learns a probabilistic mapping between conditions and waveforms. It provides seismic inputs for structural analysis that match response spectra and energy evolution while supporting uncertainty quantification via conditional diversity sampling.

## ACKNOWLEDGMENTS

This work was completed in collaboration with the Intelligent Computing Center of Jianghan University.

## CONFLICT OF INTEREST STATEMENT

The authors declare no conflicts of interest.

## DATA AVAILABILITY STATEMENT

The NGA-West2 database used in this study is available from the Pacific Earthquake Engineering Research Center (<https://peer.berkeley.edu/research/data-sciences/databases>, last accessed May 2024).

## References

1. Baker JW, Allin Cornell C. Spectral Shape, Epsilon and Record Selection. *Earthquake Engineering & Structural Dynamics*. 2006;35(9):1077–1095. doi: 10.1002/eqe.571
2. Lin T, Haselton CB, Baker JW. Conditional Spectrum-Based Ground Motion Selection. Part I: Hazard Consistency for Risk-Based Assessments. *Earthquake Engineering & Structural Dynamics*. 2013;42(12):1847–1865. doi: 10.1002/eqe.2301
3. Ancheta TD, Darragh RB, Stewart JP, et al. NGA-West2 Database. *Earthquake Spectra*. 2014;30(3):989–1005. doi: 10.1193/070913EQS197M
4. Scanlan RH, Sachs K. Earthquake Time Histories and Response Spectra. *Journal of the Engineering Mechanics Division*. 1974;100(4):635–655. doi: 10.1061/JMCEA3.0001911
5. Kaul MK. Spectrum-Consistent Time-History Generation. *Journal of the Engineering Mechanics Division*. 1978;104(4):781–788. doi: 10.1061/JMCEA3.0002379

6. Al Atik L, Abrahamson N. An Improved Method for Nonstationary Spectral Matching. *Earthquake Spectra*. 2010;26(3):601–617. doi: 10.1193/1.3459159
7. Zhang H, Yu D, Li G, Dong Z. A Ground Motion Construction Method Considering Spectrum Characteristics as Supplement for Conditional Mean Spectrum. *Bulletin of Earthquake Engineering*. 2025;23(2):579–603. doi: 10.1007/s10518-024-02084-8
8. Spanos PD, Failla G. Evolutionary Spectra Estimation Using Wavelets. *Journal of Engineering Mechanics*. 2004;130(8):952–960. doi: 10.1061/(ASCE)0733-9399(2004)130:8(952)
9. Wang D, Yu F, Kong F, Xu J. Simulation of Fully Nonstationary Random Processes Using Generalized Harmonic Wavelets. *Mechanical Systems and Signal Processing*. 2022;181:109468. doi: 10.1016/j.ymssp.2022.109468
10. Genovese F, Palmeri A. Wavelet-Based Generation of Fully Non-Stationary Random Processes with Application to Seismic Ground Motions. *Mechanical Systems and Signal Processing*. 2025;223:111833. doi: 10.1016/j.ymssp.2024.111833
11. Yamamoto Y, Baker JW. Stochastic Model for Earthquake Ground Motion Using Wavelet Packets. *Bulletin of the Seismological Society of America*. 2013;103(6):3044–3056. doi: 10.1785/0120120312
12. Huang D, Wang Z. Wavelet-based Stochastic Model for Jointly Simulating Three-component Ground Motions. *Bulletin of the Seismological Society of America*. 2022;112(3):1483–1501. doi: 10.1785/0120200290
13. Wang Z, Huang D. Stochastic Simulation of Pulse-like Ground Motions Using Wavelet Packets. *Bulletin of the Seismological Society of America*. 2024;114(4):2172–2185. doi: 10.1785/0120230190
14. Ni SH, Xie WC, Pandey M. Application of Hilbert-Huang Transform in Generating Spectrum-Compatible Earthquake Time Histories. *International Scholarly Research Notices*. 2011;2011(1):563678. doi: 10.5402/2011/563678
15. Ni SH, Xie WC, Pandey MD. Tri-Directional Spectrum-Compatible Earthquake Time-Histories for Nuclear Energy Facilities. *Nuclear Engineering and Design*. 2011;241(8):2732–2743. doi: 10.1016/j.nucengdes.2011.06.014
16. Huang D, Wang G. Energy-Compatible and Spectrum-Compatible (ECSC) Ground Motion Simulation Using Wavelet Packets. *Earthquake Engineering and Structural Dynamics*. 2017;46(11):1855–1873. doi: 10.1002/eqe.2887
17. Jin C, Hu J. A New Ground-Motion Simulation Procedure Based on Feature Extraction Matching Multiple Intensity Measures. *Soil Dynamics and Earthquake Engineering*. 2023;168:107856. doi: 10.1016/j.soildyn.2023.107856
18. Kingma DP, Welling M. Auto-Encoding Variational Bayes. arXiv preprint arXiv:1312.6114; 2013
19. Goodfellow II, Pouget-Abadie J, Mirza M, et al. Generative Adversarial Networks. arXiv preprint arXiv:1406.2661; 2014
20. Ho J, Jain A, Abbeel P. Denoising Diffusion Probabilistic Models. In: . 33. Neural Information Processing Systems (NeurIPS). Curran Associates, Inc. 2020:6840–6851.
21. Paolucci R, Gatti F, Infantino M, Smerzini C, Güney Özcebe A, Stupazzini M. Broadband Ground Motions from 3D Physics-based Numerical Simulations Using Artificial Neural Networks. *Bulletin of the Seismological Society of America*. 2018;108(3A):1272–1286. doi: 10.1785/0120170293
22. Gatti F, Clouet D. Towards Blending Physics-Based Numerical Simulations and Seismic Databases Using Generative Adversarial Network. *Computer Methods in Applied Mechanics and Engineering*. 2020;372:113421. doi: 10.1016/j.cma.2020.113421
23. Aquib TA, Mai PM. Broadband Ground-Motion Simulations with Machine-Learning-Based High-Frequency Waves from Fourier Neural Operators. *Bulletin of the Seismological Society of America*. 2024. doi: 10.1785/0120240027
24. Florez MA, Caporale M, Bubathong P, Ross ZE, Asimaki D, Meier MA. Data-driven Synthesis of Broadband Earthquake Ground Motions Using Artificial Intelligence. *Bulletin of the Seismological Society of America*. 2022;112(4):1979–1996. doi: 10.1785/0120210264
25. Esfahani RDD, Cotton F, Ohrnberger M, Scherbaum F. TFCGAN: Nonstationary Ground-motion Simulation in the Time–Frequency Domain Using Conditional Generative Adversarial Network (CGAN) and Phase Retrieval Methods. *Bulletin of the Seismological Society of America*. 2023;113(1):453–467. doi: 10.1785/0120220068
26. Huang Y, Yang C, Sun X, You J, Lu D. Ground-Motion Simulations Using Two-Dimensional Convolution Condition Adversarial Neural Network(2D-cGAN). *Soil Dynamics and Earthquake Engineering*. 2024;178:108444. doi: 10.1016/j.soildyn.2023.108444
27. Kim J, Kim B. Generative Adversarial Network to Produce Numerous Artificial Accelerograms with Pseudo-Spectral Acceleration as Conditional Input. *Computers and Geotechnics*. 2024;174:106566. doi: 10.1016/j.compgeo.2024.106566
28. Miao Y, Kang H, Hou W, Liu Y, Zhang Y, Wang C. A Response-compatible Ground Motion Generation Method Using Physics-guided Neural Networks. *Computer-Aided Civil and Infrastructure Engineering*. 2024;39(15):2350–2366. doi: 10.1111/mice.13194
29. Hu X, Chen S, Ding Y, Fu L, Li X. Spectrum-Compatible Artificial Accelerograms via Conditional Variational Autoencoder with Generative Adversarial Networks. *Engineering Structures*. 2026;348:121766. doi: 10.1016/j.engstruct.2025.121766

30. Shen J, Ni B, Ding Y, Xiong J, Zhong Z, Chen J. Aftershock Ground Motion Prediction Model Based on Conditional Convolutional Generative Adversarial Networks. *Engineering Applications of Artificial Intelligence*. 2024;133:108354. doi: 10.1016/j.engappai.2024.108354

31. Xu Z, Shen J, Wu H, Chen J. Mainshock–Aftershock Sequence Simulation via Latent Space Encoding of Generative Adversarial Networks. *Computer-Aided Civil and Infrastructure Engineering*. 2024;mice.13348. doi: 10.1111/mice.13348

32. Ren P, Nakata R, Lacour M, et al. Learning Physics for Unveiling Hidden Earthquake Ground Motions via Conditional Generative Modeling. arXiv preprint arXiv:2407.15089; 2024

33. Song J, Meng C, Ermon S. Denoising Diffusion Implicit Models. arXiv preprint arXiv:2010.02502; 2022

34. Rombach R, Blattmann A, Lorenz D, Esser P, Ommer B. High-Resolution Image Synthesis with Latent Diffusion Models. arXiv preprint arXiv:2112.10752; 2021

35. Zhang L, Rao A, Agrawala M. Adding Conditional Control to Text-to-Image Diffusion Models. arXiv preprint arXiv:2302.05543; 2023

36. Du P, Parikh MH, Fan X, Liu XY, Wang JX. Conditional Neural Field Latent Diffusion Model for Generating Spatiotemporal Turbulence. *Nature Communications*. 2024;15(1):10416. doi: 10.1038/s41467-024-54712-1

37. Li Z, Han W, Zhang Y, et al. Learning Spatiotemporal Dynamics with a Pretrained Generative Model. *Nature Machine Intelligence*. 2024;6(12):1566–1579. doi: 10.1038/s42256-024-00938-z

38. Gao H, Han X, Fan X, et al. Bayesian Conditional Diffusion Models for Versatile Spatiotemporal Turbulence Generation. *Computer Methods in Applied Mechanics and Engineering*. 2024;427:117023. doi: 10.1016/j.cma.2024.117023

39. Wang Z, Chen Y, Wang N, Chen G, Zhang D. Generative Subsurface Flow Modeling with Pretrained Diffusion Model and Training-Free Knowledge Alignment. *Geophysical Research Letters*. 2025;52(22):e2025GL118000. doi: 10.1029/2025GL118000

40. Bergmeister A, Palgunadi KH, Bosisio A, et al. High Resolution Seismic Waveform Generation Using Denoising Diffusion. arXiv preprint arXiv:2410.19343; 2024

41. Bi Z, Nakata N, Nakata R, Ren P, Wu X, Mahoney MW. Advancing Data-Driven Broadband Seismic Wavefield Simulation with Multiconditional Diffusion Model. *IEEE Transactions on Geoscience and Remote Sensing*. 2025;63:1–9. doi: 10.1109/TGRS.2025.3591881

42. Huang Y, Sun X, You J, Yang C, Lu D, Zhang J. Ground-Motion Generations Using Multi-Label Conditional Embedding–Conditional Denoising Diffusion Probabilistic Model (ML–cDDPM). *Soil Dynamics and Earthquake Engineering*. 2025;191:109274. doi: 10.1016/j.soildyn.2025.109274

43. Jung J, Lee J, Jung C, Kim H, Jung B, Lee D. Broadband Ground Motion Synthesis by Diffusion Model with Minimal Condition. arXiv preprint arXiv:2412.17333; 2025

44. Karras T, Aittala M, Aila T, Laine S. Elucidating the Design Space of Diffusion-Based Generative Models. arXiv preprint arXiv:2206.00364; 2022

45. Vaswani A, Shazeer N, Parmar N, et al. Attention Is All You Need. In: NIPS’17. Neural Information Processing Systems (NeurIPS). Curran Associates Inc. 2017; Red Hook, NY, USA:6000–6010.

46. Ronneberger O, Fischer P, Brox T. U-Net: Convolutional Networks for Biomedical Image Segmentation. In: Navab N, Hornegger J, Wells WM, Frangi AF., eds. *Medical Image Computing and Computer-assisted Intervention – MICCAI 2015* Medical Image Computing and Computer-Assisted Intervention (MICCAI). Springer International Publishing 2015; Cham:234–241

47. Xu Z, Chen J. High-Resolution Ground Motion Generation with Time–Frequency Representation. *Bulletin of Earthquake Engineering*. 2024;22(8):3703–3726. doi: 10.1007/s10518-024-01912-1

48. Daubechies I. Orthonormal Bases of Compactly Supported Wavelets. *Communications on Pure and Applied Mathematics*. 1988;41(7):909–996. doi: 10.1002/cpa.3160410705

49. Coifman R, Wickerhauser M. Entropy-Based Algorithms for Best Basis Selection. *IEEE Transactions on Information Theory*. 1992;38(2):713–718. doi: 10.1109/18.119732

50. Song Y, Dhariwal P, Chen M, Sutskever I. Consistency Models. arXiv; 2023

51. Song Y, Dhariwal P. Improved Techniques for Training Consistency Models. arXiv; 2023

52. Salimans T, Ho J. Progressive Distillation for Fast Sampling of Diffusion Models. arXiv; 2022